Green Chemistry

PAPER

View Article Online
View Journal | View Issue

Cite this: *Green Chem.*, 2025, **27**, 13375

Electrochemical reduction of ammonia-captured CO_2 to CO over a nickel single-atom catalyst

Sujin Kang, [a] Lun An, [b] Tianlei Li,[a] Long Qi, [b] Wenyu Huang [b,c] and Wenzhen Li *[a]

Received 20th May 2025,
Accepted 2nd September 2025

DOI: 10.1039/d5gc02515j

rsc.li/greenchem

Carbon reactive capture and conversion offers a sustainable route to valuable chemicals and fuels while aiding Green House Gas (GHG) reduction. Direct electrochemical conversion of capture solutions like bicarbonate avoids the energy demands of conventional CO_2 regeneration. Ammonium bicarbonate (NH_4HCO_3) is particularly attractive due to its low decomposition temperature and ability to supply *in situ* CO_2 from dilute sources without requiring purified CO_2. Meanwhile, single-atom catalysts (SACs) with nitrogen-coordinated metal sites further enhance CO_2 reduction efficiency using Earth-abundant materials. In this study, we demonstrate a nickel single-atom catalyst (Ni-SAC)-based electrolyzer that utilizes NH_4HCO_3 as the CO_2 source, achieving significantly improved CO production performance compared to the conventional silver cathodes used in the CO_2 reduction reaction (CO_2RR) to produce CO. The Ni-SAC cathode exhibited a Faradaic efficiency of 60.1% for CO production at −200 mA cm^{-2}, while the silver cathode achieved a Faradaic efficiency of only 2%, likely due to ammonium-induced poisoning. Furthermore, the integration of a customized microporous layer onto the electrode significantly increased the Faradaic efficiency from 64% to 83% at −100 mA cm^{-2}, emphasizing the crucial role of electrode structure optimization in enhancing CO selectivity. These findings demonstrate a sustainable and economically viable strategy for green CO production directly from CO_2 capture solutions.

Green foundation

1. Our work advances reactive carbon capture by integrating CO_2 capture from dilute sources with electrocatalytic conversion to CO using Earth-abundant materials, reducing dependence on energy-intensive purification and precious metals.
2. We achieved a Faradaic efficiency of 83% for CO production using a Ni single-atom catalyst (Ni-SAC) in ammonium bicarbonate media, significantly outperforming conventional Ag cathodes, which suffered from NH_4^+ poisoning.
3. Future research could enhance sustainability by integrating renewable NH_3 sources, improving Ni-SAC synthesis *via* greener precursors, and scaling the RCC-electrolysis system powered by renewable electricity.

Introduction

The development of efficient carbon capture and utilization (CCU) technologies has been recoganized as a critical strategy for achieving a carbon-neutral economy.[1] Among them, the electrochemical CO_2 reduction reaction (CO_2RR) driven by renewable electricity offers a promising approach for converting CO_2 into valuable products. However, most electrochemical CO_2RR studies have focused on pure gas-phase CO_2 feed systems, despite their high cost and significant energy demands.[2,3] This is particularly concerning given that direct air capture (DAC) can account for up to 90% of the total energy consumption in the capture process, primarily due to the CO_2 regeneration and compression steps.[4,5] A promising alternative is the direct electrochemical conversion of CO_2 from an aqueous carbon-captured solution, enabling the production of valuable products *via* the *in situ* release of CO_2 (*i*-CO_2).[3,6] This strategy can substantially reduce the overall energy requirement, approximately ~100 kJ mol^{-1} CO_2, by eliminating the need for energy-intensive CO_2 regeneration.[7]

Organic amine systems and (bi)carbonate-based systems have been proposed for CO_2 capture and subsequent reduction. However, the amine-based media face several challenges, including the difficulty of cleaving the C–N bond in carbamate[8] and the limited scalability of aqueous amine

[a]*Department of Chemical Biological Engineering, Iowa State University, 618 Bissell Road, Ames, IA 50011, USA. E-mail: wzli@iastate.edu*
[b]*U.S. DOE Ames National Laboratory, Iowa State University, 2408 Pammel Drive, Ames, IA 50011, USA*
[c]*Department of Chemistry, Iowa State University, 2415 Osborn Drive, Ames, IA 50011, USA*

absorption, which restricts their use primarily to coal or natural gas power plants.[9] In contrast, bicarbonate-based systems offer lower energy consumption and reduced environmental impact, owing to their lower heat of adsorption/absorption (~40 kJ mol^{-1}) compared to that of amines (~60–90 kJ mol^{-1}).[10,11] Significant efforts have been made to advance catalyst design,[12–14] optimize the local reaction environment,[15] and elucidate cation effects[16] in bicarbonate electrolysis systems, with much of the focus centred on potassium bicarbonate ($KHCO_3$) electrolysis for CO and formate production.[17–19] However, generating $KHCO_3$ during the carbon capture typically requires the use of a strong alkali, namely potassium hydroxide (KOH), which can pose environmental contamination risks. NH_3 offers several advantages in terms of environmental manageability and process integration. NH_3-based processes typically produce less corrosive and more recyclable waste streams due to efficient solvent regeneration, whereas spent KOH solutions require energy-intensive neutralization to mitigate the risk of persistent high-pH contamination. Therefore, under well-controlled conditions, NH_3 serves as a more environmentally manageable and regenerative alternative.

The U.S. DOE has proposed investing in a new integrated strategy known as reactive capture and conversion (RCC), which combines CO_2 capture from dilute CO_2 gas streams with its conversion into value-added products, thereby eliminating the need for a purified CO_2 intermediate stream.[20] We propose that ammonium bicarbonate can serve as a pivotal chemical medium to enable an efficient RCC process by capturing diluted CO_2 using green ammonia and subsequently upgrading it into valuable carbon chemicals. Ammonia is the second largest chemical commodity, with annual production exceeding 6 million tons,[21] and green NH_3 can be synthesized from common agricultural and industrial nitrogen wastes. A sustainable approach for upcycling waste nitrogen (NO_3^-–N) through low-concentration NO_3^- electrodialysis has been demonstrated, successfully producing NH_3 *via* electrochemical NO_3^- reduction.[22] Utilizing NH_3 as a reactive CO_2 capturing agent presents a more economical and environmentally friendly alternative. Notably, NH_4HCO_3 requires significantly less energy to release CO_2 due to its lower thermal decomposition temperature of 36 °C compared to 150 °C for $KHCO_3$.[23] In addition, the market price of NH_3 (USD 0.46 per kg)[24] is substantially lower than that of KOH (USD 0.91 per kg)[25] or monoethanolamine (MEA, USD 1.57 per kg),[26] and NH_3 exhibits lower toxicity compared to KOH.[23]

Currently, extensive research has focused on noble metal-based electrocatalysts, such as gold and silver, for the CO_2RR to produce CO, including their application in bicarbonate electrolysis systems.[12,16,27–29] However, these catalysts are not economically feasible for large-scale implementation. This presents a major challenge for using ammonia as a carbon-capture medium, as NH_4^+ is inevitably produced during the neutralization of acidic gas CO_2. In recent years, single metal site catalysts, coordinated with nitrogen ligands and embedded in carbon supports, have emerged as a promising alternative.[30–33] Among these, the Ni single atom catalyst (Ni-SAC) has gained enormous attention due to its remarkable CO_2RR activity and CO selectivity compared to conventional metal catalysts.[14,30,31,34,35] This novel electrocatalyst overcomes the limitations of the aforementioned noble catalysts. Remarkably, unlike bulk nickel catalysts, the Ni-SAC has demonstrated greater resistance to poisoning in organic amine-rich environments,[36] suggesting its potential suitability for ammonia-mediated carbon capture and reduction.

Herein, we studied the CO_2RR to produce CO in a bipolar membrane (BPM)-based membrane electrode assembly (MEA) electrolyzer employing a Ni-SAC as the cathode catalyst and NH_4HCO_3 as the reactive CO_2 medium. We demonstrated that NH_4HCO_3 can effectively serve as a reactive medium for CO_2 reduction to CO, achieving a high Faradaic efficiency (FE). The Ni-SAC outperformed a commercial silver nanoparticle (Ag-NP) catalyst in NH_4HCO_3 electrolysis, exhibiting superior resistance to NH_4^+ poisoning. By optimizing the Ni-SAC electrode structure and operating conditions, including substrate architecture and operating temperature, we achieved a FE_{CO} of 60.1% at a current density of −200 mA cm^{-2}, along with a stable operation for 10 hours at −50 mA cm^{-2}. Continuous regeneration of HCO_3^- and pH stabilization by sparging CO_2 gas into NH_4HCO_3 solution further contributed to the sustained performance of the electrolysis system.

Experimental

Materials

Nickel(II) acetylacetonate (95%), carbon tetrachloride (99.9%), and ethylenediamine (99.5%) were purchased from Millipore-Sigma. Trace-metal grade hydrochloric acid (HCl) and hydrofluoric acid (HF) were purchased from Fisher Scientific. Carbon paper (Sigracet 39BB and Freudenberg H23), an anion exchange ionomer (Sustainion XA-9 Ionomer, 5 wt%), and a bipolar membrane (Fumasep FBM) were purchased from the Fuel Cell Store. Isopropanol, carbon black (acetylene, 100% compressed), cesium bicarbonate ($CsHCO_3$, 99.99%), lithium carbonate (Li_2CO_3, 99%), potassium bicarbonate ($KHCO_3$, 99.7%), potassium carbonate (K_2CO_3, 99.7%), potassium hydroxide (KOH, >85%), and sodium bicarbonate ($NaHCO_3$, 99%) were purchased from Thermo Scientific Chemicals. Silver nanoparticles (Ag, 20 nm) and polytetrafluoroethylene (PTFE, 30–50 nm) were purchased from US Nano and Nanoshel, respectively. Ammonia solution (NH_4OH, 32%, EMPLURA) and ammonium bicarbonate (NH_4HCO_3, ≥99.0%) were purchased from Sigma-Aldrich. All purchased materials were used as received without any additional purification steps.

Synthesis of Ni-SACs

To a 50 mL round-bottom flask, 1.8 g of ethylenediamine was introduced, followed by the addition of 25–100 mg of nickel acetylacetonate ($Ni(acac)_2$). $Ni(acac)_2$ was selected as the nickel precursor due to the presence of acetylacetonate (acac) ligands, which enhance its solubility in carbon tetrachloride (CCl_4)

during the synthesis. The mixture was stirred for 5 minutes before 4.0 g of CCl_4 was added, and stirring was continued for an additional 5 minutes. Subsequently, 0.8 g of silica template (SBA-15) was introduced, and the mixture was refluxed at 90 °C for 16 hours. SBA-15 was synthesized according to the literature procedure.[37] After refluxing, the mixture was dried at 120 °C to evaporate any remaining carbon tetrachloride and ethylenediamine. The resultant residue was then calcined under an Ar atmosphere at 800 °C for 2 hours, with a ramping rate of 3 °C min^{-1}. The black powder obtained was dispersed in a solution of 5 wt% HF and 10 wt% HCl (35 mL), which was stirred for 24 hours. Centrifugation was employed to collect the catalyst, which was then washed several times with deionized water until a neutral pH was achieved. Finally, the black powder was dried at 80 °C overnight and stored for future use.

Fabrications of catalysts and electrodes

The process of making Ag and Ni-SAC electrodes for a gas-diffusion electrode (GDE) system involved spray-coating an electrocatalyst ink onto the carbon substrate surface. The ink was prepared by dispersing 40 mg of Ag or Ni-SAC powder with 8 mL of isopropanol and 250 mg of Sustainion solution, followed by sonication for 30 minutes. This ink was then deposited onto the carbon paper at 100 °C (catalyst loading: 1 mg cm^{-2}). The catalyst loading was determined by comparing the electrode's weight before and after the spray-coating process. The modified carbon substrate was prepared by depositing an additional microporous layer (MPL) onto the commercial hydrophobic carbon paper (Sigracet 39BB). The ink for MPL was prepared by mixing carbon black and PTFE with different concentrations in the ionomer solution, with a ratio of 1 : 4 in isopropanol, followed by sonication for 30 minutes. This ink was then deposited onto the carbon paper at 100 °C. The MPL loading was determined by comparing the electrode's weight before and after the spray-coating process.

Characterization studies

Aberration-corrected HAADF STEM imaging was performed using a probe-corrected Thermo Fisher (FEI) Titan Themis. Scanning electron microscopy (SEM) images and energy dispersive spectroscopy (EDS) data were collected using an FEI Quanta 250 FE-SEM. High-angle annular dark-field scanning transmission electron microscopy (HAADF-STEM) and energy-dispersive X-ray spectroscopy (EDS) mapping were performed using a Thermo Fisher Scientific Talos F200X S/TEM operated at 200 kV and equipped with a super-X EDS system. X-ray diffraction (XRD) was performed on a Rigaku SmartLab diffractometer with copper K-α radiation (λ = 0.15418 nm), operating at 40 kV and 44 mA over the 2θ range of 10 to 50 degrees. Nitrogen sorption isotherms were obtained using the Micromeritics 3Flex analyzer at −196 °C. The specific surface area was calculated with the Brunauer–Emmett–Teller (BET) model. The pore volume and pore size distribution were calculated by the Barrett–Joyner–Halenda (BJH) method. Before recording the N_2 sorption isotherms, the samples were pretreated at 200 °C under high vacuum for 12 hours. Inductively coupled plasma optical emission spectroscopy (ICP-OES) for nickel loadings was performed using an Agilent 5800 spectrometer. The NH_3-TPD experiments were conducted on a Micromeritics AutoChem II 2920. Sessile drop contact angles of deionized water in the air were measured using a ramé-hart Model 90 goniometer using a German-made U3 Series digital camera and an LED light source. We used a 1–25 μL volume manual syringe to dispense 10 ± 0.2 μL of liquid. To measure contact angles on the GDEs after use in the CO_2RR, the electrolyzer was disassembled and the GDE was rinsed with deionized water to remove residual electrolyte from the testing surface.

Bicarbonate electrolysis measurements

The flow electrolyzer contains two flow-field plates with serpentine channels, silicone gaskets, and a MEA containing two electrodes and a bipolar membrane (BPM), which was formed after assembling the cell hardware. The anode and cathode flow plates were made of titanium and stainless steel, respectively. The catholyte, 200 mL of 2.5 M of CO_2-capturing solution, was circulated through a peristaltic pump (Masterflex® L/S®) at 30 mL min^{-1}. On the anode side, 40 mL of 1.0 M KOH was circulated at 25 mL min^{-1}. The prepared sprayed electrode and a piece of Ni foam with a geometric area of 5 cm^2 were used as the cathode and anode, respectively. Argon (99.99%) was flowed into the headspace of the catholyte at 160 mL min^{-1} for the online collection and quantification of gaseous products (CO, H_2, and CO_2) *via* a gas chromatograph (GC, Agilent 8890). The temperature of the flow cell was controlled using a 50-watt 110 V heater (Dioxide Materials). The system with the CO_2 supply was operated with 80 mL of 2.5 M NH_4HCO_3 solution for the catholyte after the CO_2 provision at 70 mL min^{-1}. The pump circulation rates of the catholyte and anolyte were the same as the system without the CO_2 supply, and argon was connected to the headspace of the catholyte at 90 mL min^{-1}. Gas products, including CO, H_2, and CO_2, were analyzed over a 30-minute duration. A thermal conductivity detector (TCD) was used to detect H_2, and a flame ionization detector (FID) was used to detect CO and CO_2 in the GC. The calibration curves for H_2 (1000–20000 ppm, Cal Gas Direct), CO (2000–20000 ppm, Cal Gas Direct), and CO_2 (2000–50000 ppm, Cal Gas Direct) were established by analyzing the calibration gases. Liquid products (*e.g.*, formate) were quantified by ion chromatography (IC, Thermo Scientific Dionex Easion). 1 mL of the sample solution was diluted with deionized water and injected into the IC for its quantification. The durability test was performed in a similar flow cell setup, and the catholyte was refreshed every 2 hours manually. The volumes of catholyte and anolyte were 250 mL and 200 mL, respectively. Gas products, including CO, H_2, and CO_2, were analyzed at one-hour intervals by averaging 4 points.

Bicarbonate and carbamate contents were determined by ^{13}C nuclear magnetic resonance (NMR) spectroscopy on a Bruker Avance III 600 MHz NMR spectrometer. 400 μL of the sample solution was mixed with 200 μL of D_2O and 100 μL of

2000 ppm DMS (dimethyl sulfone) solution for the internal standard. The scan number was 1024. A calibration range of 0–2.5 M was utilized for $KHCO_3$ and K_2CO_3, and ammonium carbamate in 1 M NH_3 solution was prepared for a calibration in the range of 0–0.5 M.

Calculations of performance

The Faradaic efficiencies of gaseous products (H_2 and CO) were calculated using the following equation:

$$FE_i = \frac{z_i \times n_i \times F}{Q} \times 100$$

where z is the number of electrons (2 for H_2 and CO) used for producing the products, n_i is the number of moles of product i (mol) in GC, F is the Faradaic constant (96485 C mol^{-1}), and Q is the total charge transferred.

During the electrochemical CO_2 reduction reaction, the solution resistance was measured by electrochemical impedance spectroscopy at each measurement for ohmic drop (iR) compensation. The ohmic drop was manually compensated at an 85% level. The applied potentials (*vs.* Ag/AgCl, $E_{Ag/AgCl}$) of the working electrode were converted to the reversible hydrogen electrode scale (E_{RHE}) using the following equation:

$$E(\mathrm{V}\,vs.\,\mathrm{RHE}) = E(\mathrm{V}\,vs.\,\mathrm{Ag/AgCl}) + 0.197 + 0.059 \times \mathrm{pH}.$$

To measure electrochemical capacitance, cyclic voltammetry (CV) was conducted within a potential window of ±500 mV, centered around the open circuit potential (OCP). The measurements were performed at varying scan rates, 10, 20, 40, 60, 80, and 100 mV s^{-1}, in a 0.1 M $KHCO_3$ solution to calculate the electrochemically active surface area (ECSA) and double layer capacitance of the Ni-SAC electrodes. For these experiments, the Ni-SAC ink sprayed on H23 was used as the working electrode, and a silver/silver chloride (Ag/AgCl) containing saturated KCl served as the reference electrode. The ECSA was calculated using the equation ECSA = C_{dl}/C_s, where C_s is the specific capacitance of a flat standard electrode. The specific capacitance for a flat surface is generally found to be in the range of 20–60 μF cm^{-2}. We assume the average value of 40 μF cm^{-2} as the specific capacitance in this work.[38] The ECSAs of the electrodes were inferred by measurements of the double-layer capacitance. The mass activity (A g^{-1}) for CO (electron transferred/mass metal/time = current/mass metal) was calculated as follows: $I_{product}/(m_{cat} \times \omega_i)$, where $I_{product}$ is the partial current for CO, m_{cat} is the catalyst mass in the electrode, and ω is the Ni loading in the catalyst.

Results and discussion

Synthesis and characterization of the Ni-SAC

The Ni-SAC was synthesized *via* a hard-templating method, involving the polymerization of ethylenediamine and carbon tetrachloride in the presence of nickel(II) acetylacetonate (Ni(acac)$_2$) within the mesopores of SBA-15.[37] Ethylenediamine served a dual role as both a ligand for the nickel precursor and a nitrogen source for the carbon matrix. The templating process was crucial in regulating the polymerization behavior, which in turn significantly influenced the morphology of the resulting Ni-SAC (Fig. 1a).[39] Following polymerization, the material was carbonized at 800 °C under an inert atmosphere, a critical step in incorporating nickel ions into the graphitic framework of the SAC support. The silica template was then etched away, releasing the Ni-SAC. This modular synthesis approach offers fine control over the catalyst properties, enabling precise tuning of the nickel content by adjusting the amount of Ni(acac)$_2$ precursor used (25–100 mg). This variation in precursor loading yielded nickel contents ranging from 1.20 to 2.08 wt%, as determined by ICP-OES (Table S1). The microstructure of the Ni-SAC was examined by using transmission electron microscopy (TEM) and high-angle annular dark-field scanning transmission electron microscopy (HAADF-STEM), as shown in Fig. 1b and c. These characterization studies confirmed the absence of nickel nanoparticles or clusters in the samples. The Ni-SAC exhibited a rod-like morphology with well-aligned mesopores averaging approximately 700 nm in length. Bright spots observed in HAADF-STEM images (highlighted by red circles) indicate that Ni atoms are uniformly dispersed throughout the carbon matrix without agglomeration. STEM-EDS mapping of the Ni-SAC confirmed

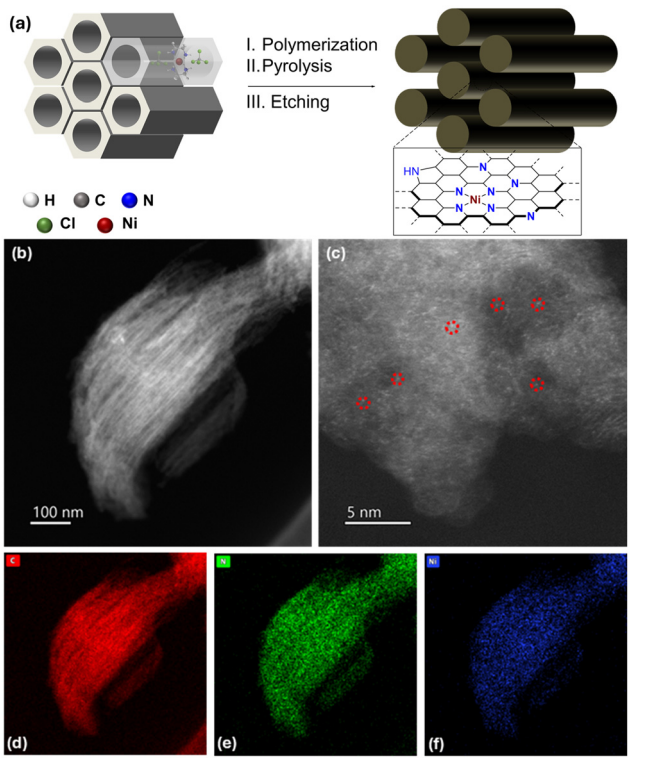

Fig. 1 Synthesis and microscopic characterization of the Ni-SAC. (a) Schematic representation of the general synthetic method for the Ni-SAC; (b, c) aberration-corrected HAADF-STEM image; (d, e, f) EDS mapping, illustrating the spatial distributions of C (red), N (green) and Ni (blue).

an even distribution of nickel and nitrogen on the carbon support (Fig. 1d–f). X-ray photoelectron spectroscopy (XPS) analysis verified the presence of carbon, nitrogen, and nickel through their characteristic signals (Fig. S1). Powder X-ray diffraction (XRD) analysis revealed two broad peaks at 27° and 43°, corresponding to the (002) and (004) planes of the N-doped carbon support (Fig. S2). Importantly, no diffraction peaks associated with crystalline nickel phases were detected, indicating the absence of nickel nanoparticles or bulk phases.

NH_4HCO_3 electrolysis on Ni-SACs and the mechanism study

The CO_2RR performance of Ag-NP and Ni-SACs was evaluated using 2.5 M $KHCO_3$ and NH_4HCO_3 solutions as carbon-capturing solutions, serving simultaneously as the electrolyte and CO_2 reactant. The Ni-SAC prepared with 100 mg of $Ni(acac)_2$ was utilized for further electrolysis. A MEA-based flow electrolyzer was employed, consisting of two flow-field plates, silicone gaskets, an anode, a cathode, and a BPM (Fig. S3). As shown in Fig. 2a, *i*-CO_2RR (*in situ* generated CO_2 reduction reaction) performance was compared at a current density of −100 mA cm^{-2}. When operated with 2.5 M $KHCO_3$ solution, the Ni-SAC catalyst achieved a high FE_{CO} of 56%, which is twice that of an Ag-NP catalyst (28%) at the same loading. The electrochemical surface area (ECSA) of the cathodes decreased after exposure to the CO_2RR, regardless of the cation species present. However, the cathode used in $KHCO_3$ electrolysis exhibited less ECSA degradation compared to that in NH_4HCO_3, as shown in Tables S2 and S3, and Fig. S4 and S5, aligning with the observed performance trends in the two electrolytes ($KHCO_3$ and NH_4HCO_3). Notably, the FE_{CO} for the Ag-NP catalyst drops to <1% when the electrolyte is switched to 2.5 M NH_4HCO_3, indicating that Ag loses its activity in NH_4^+ abundant environments. In sharp contrast, the Ni-SAC electrode retained a FE_{CO} of 42.3%, an unexpected behaviour considering that NH_4^+ adsorption is stronger on Ag than on Ni. Control experiments using nickel nanoparticles (Ni-NPs) and nitrogen-doped carbon (N–C) without isolated Ni sites, at the same loadings, showed negligible CO production, highlighting the critical role of atomically dispersed Ni in the observed activity. We observed that the FE_{CO} from the CO_2RR using 2.5 M NH_4HCO_3 was lower compared to that with 2.5 M $KHCO_3$ (54.5%). This suggests a distinct behavior of Ni-SAC in NH_4^+-rich environments, differing from typical reports of ammonia-induced catalyst poisoning. Further investigation, including detailed characterization and theoretical work, is needed to better understand the NH_4^+ tolerance mechanism of Ni-SAC.[40] Additionally, the calculated mass activity of Ni-SAC reached 5886 and 4557 A g^{-1} under K^+ and NH_4^+ abundant systems, respectively, which is higher than those of Ag (2696 and 183 A g^{-1}), as shown in Fig. S6.

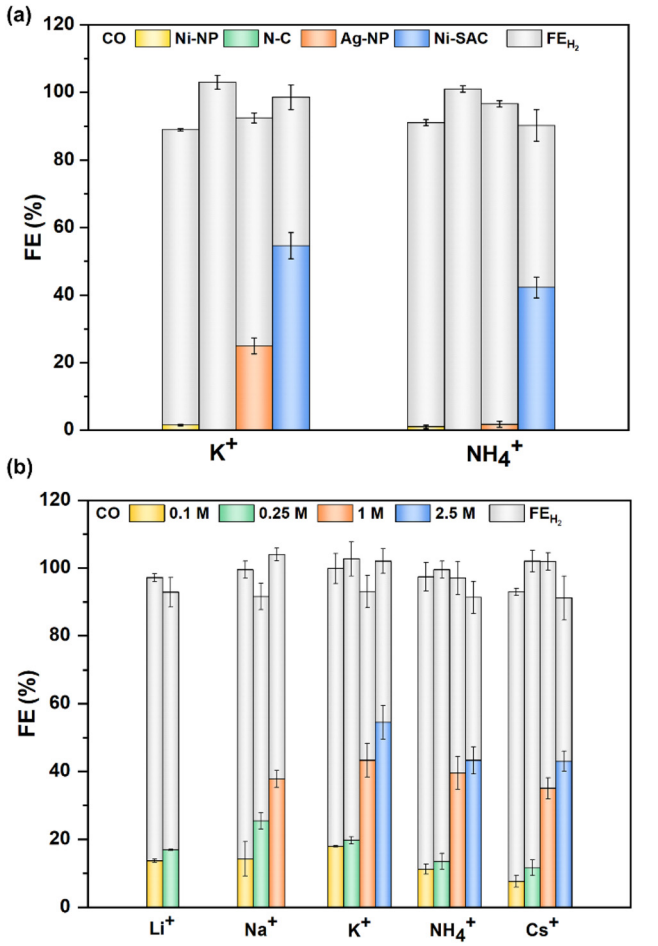

Fig. 2 FE comparisons between different catalysts and in various cation environments. (a) FE comparison between Ni-NP, N-C, Ag-NP and Ni-SAC in 2.5 M $KHCO_3$ and NH_4HCO_3 catholytes (carbon paper: Freudenberg H23, current density: −100 mA cm^{-2}, temperature: RT, catalyst loading: 1 mg cm^{-2}), and (b) FE of the Ni-SAC in bicarbonate electrolytes containing different alkali cations (concentration : 0.1 M ~ 2.5 M).

To investigate the effects of different cations, we experimentally evaluated bicarbonate electrolytes containing various metal cations (Li^+, Na^+, K^+, and Cs^+) and the ammonium cation (NH_4^+). Interestingly, both the FE_{CO} (Fig. 2b) and partial current density j_{CO} (Fig. S7) on the Ni-SAC were found to be less influenced by the effective cation size compared to changes in bicarbonate concentration. This suggests that CO_2RR performance on the Ni-SAC is relatively insensitive to the type of cation present, in sharp contrast to previously reported trends for Ag electrodes, where a larger cation has been shown to enhance FE_{CO} through stronger interfacial effects.[16] The concentration of the bicarbonate catholyte solutions significantly influenced performance, with higher concentrations yielding superior CO selectivity compared to lower ones. Such marginal cation dependence may be associated with the positively shifted point of zero charge (PZC) of the Ni-SAC, which allows for effective cation accumulation and stabilization of $CO_2^{\bullet-}$ intermediates even in the presence of strongly hydrated cations such as Li^+.[36] Based on these results, we conclude that the Ni-SAC exhibits only a marginal cation effect, and its weak cation sensitivity enables selective CO_2RR across a wide range of absorbent media.

Optimization of electrode and operation conditions for NH_4HCO_3 electrolysis

The effect of temperature on CO_2RR activity was also investigated, as temperature influences both CO_2 regeneration from bicarbonate and the kinetics of the CO_2RR and HER, making the determination of the optimal operating temperature challenging.[16] Increasing the temperature of the system accelerates the CO_2 regeneration rate from bicarbonate. While the production rates of both CO and H_2 increase with temperature, the extent of this enhancement differs due to their distinct activation energy barriers.[36] The CO production was evaluated across cell temperatures from 25 °C to 60 °C at a current density of −100 mA cm^{-2}, as shown in Fig. 3a. Elevated temperatures are anticipated to enhance CO_2 generation by accelerating the dissociation of bicarbonate: $HCO_3^- \rightarrow OH^- + CO_2$. Notably, at around 40 °C, NH_4HCO_3 begins to thermally decompose to generate *i*-CO_2 (decomposition onset at 36 °C), providing a greater supply of *i*-CO_2 compared to lower temperatures, such as 25 °C. Up to 40 °C, CO production increased with temperature (42.3% *vs.* 56.8%); however, at 60 °C, CO selectivity declined to 45.5% due to the rapid rise in H_2 generation, consistent with trends reported in previous studies.[36] The temperature dependence of FE_{CO} follows a trend similar to that observed in systems using carbamate solutions.[36] Additionally, increasing temperature raises the surface pH,[15] which can facilitate carbonate generation and consequently reduce FE_{CO}. The effect of catalyst loading (0.5, 1, and 2 mg cm^{-2}) on the CO and H_2 distribution was also examined (Fig. 3b). At 40 °C and −100 mA cm^{-2}, increasing the catalyst loading from 0.5 to 1 mg cm^{-2} boosted the FE_{CO} from 49.6% to 64.3%. However, a further catalyst loading increase to 2 mg cm^{-2} did not improve the CO_2RR performance, with FE_{CO}: 64.3% slightly dropping to 59.5%.

The characteristics of the GDE, including its hydrophobicity and thickness, were further optimized to enhance the CO_2 reduction reactions.[41,42] It was found that adjusting the gas diffusion layer and surface properties can significantly influence bicarbonate electrolysis for CO production. To further improve captured CO_2RR performance over Ni-SACs, surface modification of the electrode was examined by varying the catalyst-to-PTFE ratio in the catalyst ink, as shown in Fig. 3c. The catalyst ink was spray-coated onto the commercial hydrophobic carbon paper (CP) (Sigracet 39BB), and CO_2RR performance was evaluated at a current density of −100 mA cm^{-2}. Optimization of PTFE and catalyst loading led to improved CO_2RR performance, with the highest FE_{CO} of 64.3% achieved when the PTFE content in the catalyst ink was 20%, outperforming other tested compositions.

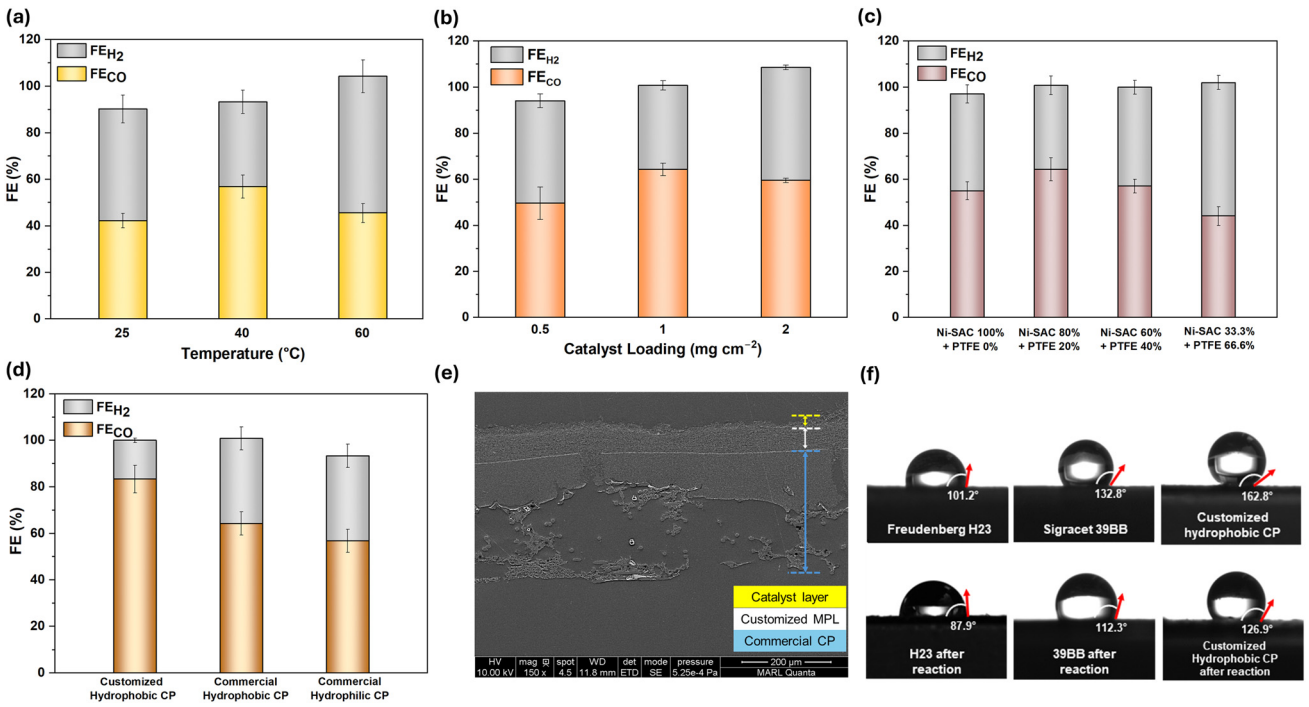

Fig. 3 Performance optimization and structural characterization of Ni-SAC electrodes. (a) FE_{CO} of the Ni-SAC in 2.5 M NH_4HCO_3 at various temperatures on hydrophilic carbon paper (Freudenberg H23), (b) FE_{CO} of Ni-SAC in 2.5 M $KHCO_3$ with different catalyst loadings at 40 °C and at a current density of −100 mA cm^{-2}, (c) with different ratios of sprayed catalyst and PTFE (CP: Sigracet 39BB) in 2.5 M $KHCO_3$. (d) FE_{CO} comparison of Ni-SAC electrodes with commercial hydrophilic, hydrophobic carbon substrates, and microporous layer-customized hydrophobic substrates (current density: −100 mA cm^{-2}) in 2.5 M NH_4HCO_3 at 40 °C. (e) SEM image of the cross-sectional area from the customized hydrophobic electrode and (f) changes in the hydrophobicity of gas diffusion electrodes (GDEs) after exposure to ammonium bicarbonate solutions under electrolysis conditions. Contact angles of commercial hydrophilic carbon paper (Freudenberg H23), hydrophobic carbon paper (Sigracet 39BB), and customized hydrophobic carbon paper before electrolysis and the same electrodes after electrolysis.

Furthermore, Fig. 3d shows that the increased hydrophobicity led to a higher FE_{CO}. The hydrophilic electrode (Freudenberg H23) achieved a FE_{CO} of 56.8%, while the commercial hydrophobic electrode (Sigracet 39BB), without additional treatment, reached 64.3% at 40 °C. This improvement is likely due to the hydrophobic microporous layer (MPL) on the hydrophobic carbon paper, which creates a favorable microenvironment for efficient gas transport. Additionally, the hydrophobic substrate helps retain gaseous reactants near the catalyst layer, promoting the formation of solid–liquid–gas interfaces that enhance both the activity and selectivity for CO_2-to-CO reduction.[32] Moreover, a customized hydrophobic GDE, featuring an additional microporous layer composed of PTFE and carbon black on commercial hydrophobic carbon paper, demonstrated enhanced performance compared to the untreated commercial hydrophobic CP (83% *vs.* 64.3%). The cross-sectional SEM image (Fig. 3e) revealed a distinct three-layered structure in the customized hydrophobic electrode, with an additional microporous layer, in contrast to the commercial hydrophobic electrode (Fig. S8). Elemental mapping of both electrodes further confirmed the presence of a well-defined microporous sublayer containing PTFE (Fig. S9 and S10).

To evaluate the hydrophobicity of the electrode surface, we measured the contact angle of water droplets on the cathode, as shown in Fig. 3f. The customized hydrophobic CP demonstrated enhanced performance (162.8°) compared to the commercial hydrophobic CP alone (132.8°). However, the hydrophobicity of the electrode layer deteriorated under CO_2RR conditions, likely due to PTFE degradation under negative potentials, consistent with previous reports.[42,43] Nevertheless, the contact angle of the customized hydrophobic CP after the electrolysis (126.9°) remained higher than that of the hydrophilic CP (101.2°) and was comparable to that of the commercial hydrophobic CP before the reaction (132.8°). These characterization results suggest that incorporating the MPL with tailored wetting properties is an efficient strategy for enhancing FE_{CO} in captured CO_2RR systems.

Bicarbonate regeneration during NH_4HCO_3 electrolysis

The effects of feeding pure CO_2 into the bicarbonate solution were investigated (Fig. S11 and S12) to evaluate the influence of carbon and nitrogen species on the CO_2RR and to improve performance in NH_3-based carbon-captured solutions, as shown in Fig. 4a and b. Notably, the CO_2-supplied system achieved a higher 60.1% of FE_{CO} at −200 mA cm^{-2} compared to 40.2% of FE_{CO} without CO_2 supplementation. Furthermore, the partial current density for CO production increased linearly with applied current, reaching −120.3 mA cm^{-2} at −200 mA cm^{-2} (Fig. S13), demonstrating enhanced CO generation under CO_2-rich conditions. In contrast, the system without CO_2 supply achieved only 40.2% FE_{CO} at −200 mA cm^{-2}, with a CO partial current density lower than that observed at −150 mA cm^{-2}. For the CO_2-supplied system, the full cell voltage (with 85% *iR* compensation) increased from 2.71 V at −50 mA cm^{-2} to 2.90 V, 3.06 V, and 3.64 V at −100, −150, and −200 mA cm^{-2}, respectively, showing modest improvements in energy efficiency compared to the system without CO_2 purging. These results are consistent with the

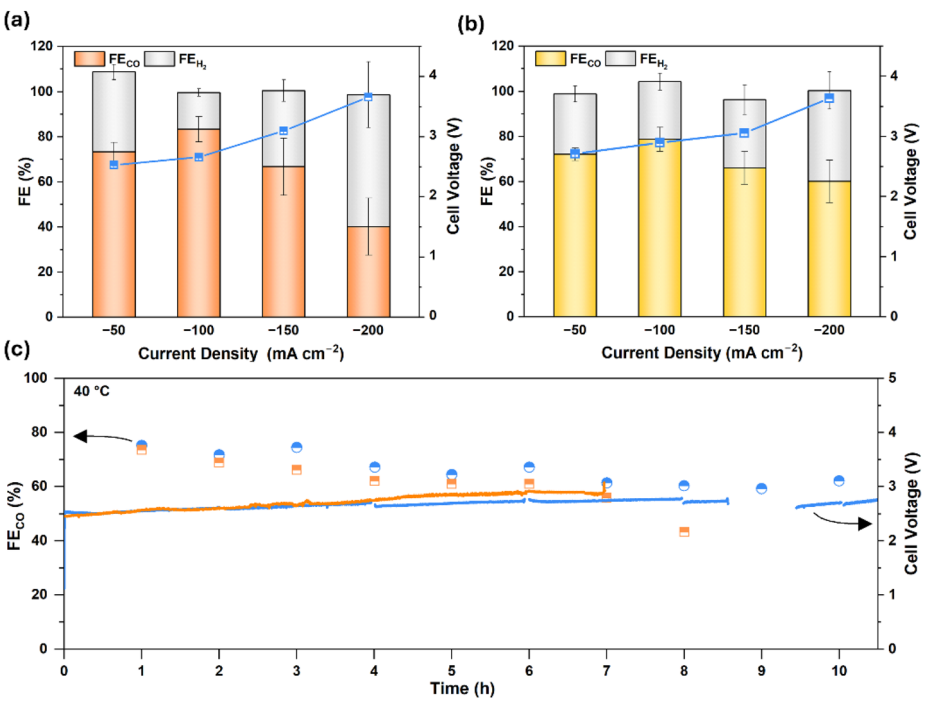

Fig. 4 FE and cell voltage profiles. (a) No CO_2 purging and (b) with CO_2 purging as a function of applied current densities (−50 ~ −200 mA cm^{-2}), and (c) the long-term durability test of the Ni-SAC in a flow cell at −50 mA cm^{-2}.

observed pH differences between the two systems after electrolysis (Table S4). The pH changes in the non-CO_2 supplied system were monitored under electrolysis at −200 mA cm^{-2}, revealing a rapid increase from 7.8 to 8.4 within 30 minutes. In contrast, the CO_2-supplied system exhibited a more gradual rise, with pH stabilizing around 8. This stabilized pH environment allowed for a mitigation of OH^- accumulation and the generation of an adequate amount of *i*-CO_2 from preserved bicarbonate. These results demonstrated that pH control plays a critical role in maintaining bicarbonate species as active reactants, thereby directly influencing the CO_2RR performance under NH_4HCO_3 conditions.

To investigate the species present in the solution and their impacts on the CO_2RR to produce CO, ^{13}C NMR spectra of the bicarbonate solutions were collected before and after electrolysis, with CO_2 gas purging applied at current densities of −100 mA cm^{-2} and −200 mA cm^{-2}. The 2.5 M NH_4HCO_3 solution spontaneously formed carbamate (system 1, Table S5) as a result of thermo-decomposition. After 30 minutes of electrolysis at −100 mA cm^{-2} (system 2), bicarbonate was partially consumed for CO production, accompanied by the generation of additional carbamate and CO_2 (Table S6). However, with a continuous CO_2 gas supply (system 3), the consumed bicarbonate in the catholyte was replenished, resulting in a bicarbonate concentration that exceeded its original level and a net positive carbon balance. A slight shift of the bicarbonate peak to higher ppm values in the ^{13}C-NMR spectra indicated carbonate formation *via* the following reaction:

$$NH_3 + HCO_3^- \rightarrow NH_4^+ + CO_3^{2-}.$$

At −200 mA cm^{-2} (system 4), bicarbonate was consumed more extensively than at −100 mA cm^{-2}, resulting in a corresponding decrease in carbamate levels. The replenishment of bicarbonate had a greater impact in system 4 than in system 3, effectively compensating for the rapid depletion of the reactant. This also accounts for the reduced carbon balance observed after electrolysis compared to system 3. To the best of our knowledge, no prior study has comprehensively quantified the behavior of ammonium bicarbonate, carbamate, and carbonate during bicarbonate electrolysis.

Long-term stability tests of the modified Ni-SAC electrode were performed at a current density of −50 mA cm^{-2} in a BPM-MEA flow cell system (Fig. 4c). In the absence of CO_2 supply, the system exhibited a gradual decline in FE_{CO} from 61% to 35.2% over 8 hours, primarily due to pH shifts in the electrolyte affecting electrode stability. In contrast, the CO_2-supplied system maintained steady CO production with FE_{CO} ranging from 60 to 70% and an average stable cell voltage of 2.7 V for 10 hours, indicating sustained NH_4HCO_3 electrolysis. After 11 hours, the FE_{CO} dropped below 60%, accompanied by a rise in cell voltage, attributed to the PTFE loss from the electrode under prolonged current operation. This led to a decline in hydrophobicity (from 162.8° to 126.9°, Fig. 3f) and increased HER activity. No significant agglomeration or formation of Ni nanoparticles was observed for the post-electrolysis Ni-SAC (Fig. S14), indicating that the catalyst deactivation is unlikely to be the main cause of the observed performance degradation. These findings highlight the importance of pH regulation and bicarbonate replenishment for stable CO_2RR performance in NH_4HCO_3 media. In addition, SEM images of the electrode surface before and after electrolysis revealed nanostructure formation that covered the catalyst surface, contributing to the observed performance degradation (Fig. S15).

To clearly assess the electrocatalytic performance of Ni-SAC, the highest FE_{CO} and corresponding cell voltages at current densities of −100 and −200 mA cm^{-2} were compared with state-of-the-art BPM-based flow cell electrolyzer systems utilizing Ni-SAC for CO_2-to-CO conversion, as summarized in Table S7. Various captured carbon sources were assessed, including MEA, $KHCO_3$, and NH_4HCO_3. At −100 mA cm^{-2}, bicarbonate electrolysis demonstrated superior FE_{CO} and lower cell voltage compared to amine-based systems, resulting in reduced energy consumption. Among the bicarbonate-based systems, $KHCO_3$ electrolysis with CO_2 supply achieved the highest energy efficiency for CO production, followed closely by CO_2-supplied NH_4HCO_3 electrolysis. $KHCO_3$ electrolysis without CO_2 supply showed lower CO production and higher cell voltage compared to the CO_2-supplied system. However, at −200 mA cm^{-2}, $KHCO_3$ electrolysis with CO_2 supply sustained a higher FE_{CO} exceeding 90%[14] at a cell voltage of 3.7 V, while CO_2-supplied NH_4HCO_3 electrolysis achieved a FE_{CO} of 60.1% at 3.64 V. As research on NH_4HCO_3 electrolysis is still in its early stages, further optimization and performance enhancements are expected.

Conclusions

NH_4HCO_3 can serve as a waste-derived reactant for electrochemical CO_2 reduction *via in situ* generated CO_2 using a Ni-SAC as the electrocatalyst. The unique properties of the Ni-SAC were systematically investigated, revealing that it has a weaker NH_4^+ adsorption energy compared to Ag, leading to a relatively unexpected resistance to NH_4^+ poisoning. Further optimization of operating conditions and electrode design, including an optimal temperature of 40 °C and the incorporation of a customized hydrophobic microporous layer, enhanced the retention of gaseous reactants near the catalyst surface. This modification of the local environment facilitated the formation of solid–liquid–gas interfaces, resulting in a FE_{CO} of 60.1% at −200 mA cm^{-2}. pH control and maintenance of bicarbonate species through continuous CO_2 supply significantly improved the FE_{CO} at higher current densities and extended the electrolysis stability up to 10 hours. To the best of our knowledge, this is an early report investigating ammonia-based reactive CO_2 capture and its electrochemical reduction to CO, providing new insights into the use of earth-abundant metal electrocatalysts for the conversion of the *in situ* generated CO_2 from NH_4HCO_3. By harnessing the highly reversible formation and decomposition of NH_4HCO_3, waste nitrogen-derived NH_3 can serve as an economical capture agent, enabling its electrochemical conversion through a reactive CO_2 capture–release cycle.

Author contributions

S. Kang and W. Li designed the experiments. S. Kang conducted XRD, SEM, coordinated XPS and TEM characterization studies and performed the electrochemical measurements and characterization. L. An synthesized the catalyst and conducted ICP-OES and BET analysis. T. Li provided important and constructive suggestions for this work. L. Qi, W. Huang, and W. Li supervised the project. S. Kang drafted the manuscript, and all authors collaborated in discussions and contributed to the manuscript's review and editing.

Conflicts of interest

There are no conflicts to declare.

Data availability

The data supporting this article have been included as part of the supplementary information (SI).

The SI contains additional figures and tables, and supporting electrochemical data for the Ni-SAC catalysts and CO_2-to-CO conversion. See DOI: **https://doi.org/10.1039/d5gc02515j**.

Acknowledgements

This work was supported by the DOE-EPSCoR (DE-SC0025376), NSF ECO-CBET (2219162), and EPSCoR FEC (2316481) grants. W. L. is grateful for his Herbert L. Stiles Professor Fellowship. L. A. and L. Q. were supported by the Laboratory-Directed Research and Development Program at the Ames National Laboratory for the Design and Synthesis of Carbon Materials. L. A. and L. Q. were supported by the U.S. Department of Energy (DOE), Office of Basic Energy Sciences, Division of Chemical Sciences, Geosciences, and Biosciences, Catalysis Science Program, for the characterization of carbon materials and data analysis. The Ames Laboratory is operated for the U.S. DOE by Iowa State University under contract no. DE-AC02-07CH11358. S. Kang is grateful to Dr Dapeng Jing and Dr Tao Ma for carrying out XPS and TEM characterization studies and acknowledges the fruitful discussion with Prof. Shuang Gu, Prof. Gang Wu, Dr Manman Qi, Dr Yifu Chen, Dr Hengzhou Liu, Dr Qiqi Mao, Xiaopeng Liu, Mohammad Albloushi, Rod Alexei De Guzman, Huu Huy Nguyen, Dr Jie Zhang, Dr Shoutian Sun, and Prof. Bin Wang.

References

1 D. U. Nielsen, X.-M. Hu, K. Daasbjerg and T. Skrydstrup, *Nat. Catal.*, 2018, **1**, 244–254.
2 D. W. Keith, G. Holmes, D. St Angelo and K. Heidel, *Joule*, 2018, **2**, 1573–1594.
3 G. Lee, A. S. Rasouli, B.-H. Lee, J. Zhang, D. H. Won, Y. C. Xiao, J. P. Edwards, M. G. Lee, E. D. Jung, F. Arabyarmohammadi, H. Liu, I. Grigioni, J. Abed, T. Alkayyali, S. Liu, K. Xie, R. K. Miao, S. Park, R. Dorakhan, Y. Zhao, C. P. O'Brien, Z. Chen, D. Sinton and E. Sargent, *Joule*, 2023, **7**, 1277–1288.
4 W. Gao, S. Liang, R. Wang, Q. Jiang, Y. Zhang, Q. Zheng, B. Xie, C. Y. Toe, X. Zhu, J. Wang, L. Huang, Y. Gao, Z. Wang, C. Jo, Q. Wang, L. Wang, Y. Liu, B. Louis, J. Scott, A. C. Roger, R. Amal, H. He and S. E. Park, *Chem. Soc. Rev.*, 2020, **49**, 8584–8686.
5 K. Zhang, D. Guo, X. Wang, Y. Qin, L. Hu, Y. Zhang, R. Zou and S. Gao, *J. CO2 Util.*, 2023, **72**, 102493.
6 Y. C. Xiao, C. M. Gabardo, S. Liu, G. Lee, Y. Zhao, C. P. O'Brien, R. K. Miao, Y. Xu, J. P. Edwards, M. Fan, J. E. Huang, J. Li, P. Papangelakis, T. Alkayyali, A. Sedighian Rasouli, J. Zhang, E. H. Sargent and D. Sinton, *EES Catal.*, 2023, **1**, 54–61.
7 W. A. Smith, T. Burdyny, D. A. Vermaas and H. Geerlings, *Joule*, 2019, **3**, 1822–1834.
8 T. Li and M. Shao, *EES Catal.*, 2024, **2**, 564–572.
9 B. Dziejarski, J. Serafin, K. Andersson and R. Krzyżyńska, *Mater. Today Sustain.*, 2023, **24**, 100483.
10 F. Shakerian, K.-H. Kim, J. E. Szulejko and J.-W. Park, *Appl. Energy*, 2015, **148**, 10–22.
11 S. E. Renfrew, D. E. Starr and P. Strasser, *ACS Catal.*, 2020, **10**, 13058–13074.
12 E. W. Lees, M. Goldman, A. G. Fink, D. J. Dvorak, D. A. Salvatore, Z. Zhang, N. W. X. Loo and C. P. Berlinguette, *ACS Energy Lett.*, 2020, **5**, 2165–2173.
13 J. Lee, H. Liu and W. Li, *ChemSusChem*, 2022, **15**, e202201329.
14 H. Song, C. A. Fernández, H. Choi, P.-W. Huang, J. Oh and M. C. Hatzell, *Energy Environ. Sci.*, 2024, **17**, 3570–3579.
15 Z. Zhang, L. Melo, R. P. Jansonius, F. Habibzadeh, E. R. Grant and C. P. Berlinguette, *ACS Energy Lett.*, 2020, **5**, 3101–3107.
16 A. G. Fink, E. W. Lees, Z. Zhang, S. Ren, R. S. Delima and C. P. Berlinguette, *ChemElectroChem*, 2021, **8**, 2094–2100.
17 M. Shen, L. Ji, D. Cheng, Z. Wang, Q. Xue, S. Feng, Y. Luo, S. Chen, J. Wang and H. Zheng, *Joule*, 2024, **8**, 1999–2015.
18 A. Yoshizawa, M. Higashi, A. Anzai and M. Yamauchi, *Energy Adv.*, 2024, **3**, 778–783.
19 Z. Zhang, D. Xi, Z. Ren and J. Li, *Cell Rep. Phys. Sci.*, 2023, **4**, 101662.
20 T. G. Deutsch, S. Baker, P. Agbo, D. R. Kauffman, J. Vickers and J. A. Schaidle, in *Summary Report of the Reactive CO2 Capture: Process Integration for the New Carbon Economy Workshop*, National Renewable Energy Laboratory (NREL), Golden, CO (United States), 2020.
21 S. Ghavam, M. Vahdati, I. A. G. Wilson and P. Styring, *Front. Energy Res.*, 2021, **9**, 580808.
22 Y. Chen, P. Ammari-Azar, H. Liu, J. Lee, Y. Xi, M. J. Castellano, S. Gu and W. Li, *EES Catal.*, 2023, **1**, 504–515.
23 H. Liu, Y. Chen, J. Lee, S. Gu and W. Li, *ACS Energy Lett.*, 2022, **7**, 4483–4489.

24 Ammonia price index. Retrieved Dec. 10, businessanalytiq.com.
25 Potassium Hydroxide price index. Retrieved Dec. 10, businessanalytiq.com.
26 Monoethanolamine price index. Retrieved Dec. 10, businessanalytiq.com.
27 W. Wang, S. Gong, H. Wang, Y. Tan, X. Zhu, X. Wang, J. Liu, W. Yu, G. Zhu and X. Lv, *Chem. Eng. J.*, 2024, **490**, 151849.
28 Z. Zhang, E. W. Lees, F. Habibzadeh, D. A. Salvatore, S. Ren, G. L. Simpson, D. G. Wheeler, A. Liu and C. P. Berlinguette, *Energy Environ. Sci.*, 2022, **15**, 705–713.
29 T. Li, E. W. Lees, M. Goldman, D. A. Salvatore, D. M. Weekes and C. P. Berlinguette, *Joule*, 2019, **3**, 1487–1497.
30 Y. Li, N. M. Adli, W. Shan, M. Wang, M. J. Zachman, S. Hwang, H. Tabassum, S. Karakalos, Z. Feng, G. Wang, Y. C. Li and G. Wu, *Energy Environ. Sci.*, 2022, **15**, 2108–2119.
31 P. Yue, K. Xiong, L. Ma, J. Li, L. Zhang, X. Zhu, Q. Fu and Q. Liao, *ACS Appl. Mater. Interfaces*, 2022, **14**, 54840–54847.
32 Z. Yin, J. Yu, Z. Xie, S. W. Yu, L. Zhang, T. Akauola, J. G. Chen, W. Huang, L. Qi and S. Zhang, *J. Am. Chem. Soc.*, 2022, **144**, 20931–20938.
33 Z. Chen, X. Zhang, W. Liu, M. Jiao, K. Mou, X. Zhang and L. Liu, *Energy Environ. Sci.*, 2021, **14**, 2349–2356.
34 Q. Fan, P. Hou, C. Choi, T. S. Wu, S. Hong, F. Li, Y. L. Soo, P. Kang, Y. Jung and Z. Sun, *Adv. Energy Mater.*, 2020, **10**, 1903068.
35 X. Qin, H. Shi, H. Li, B. Chu, J. Zhang, Z. Wen, X. Sun, H. Wang and Y. He, *Nat. Commun.*, 2025, **16**, 33.
36 J. H. Kim, H. Jang, G. Bak, W. Choi, H. Yun, E. Lee, D. Kim, J. Kim, S. Y. Lee and Y. J. Hwang, *Energy Environ. Sci.*, 2022, **15**, 4301–4312.
37 Z. Luo, Z. Yin, J. Yu, Y. Yan, B. Hu, R. Nie, A. F. Kolln, X. Wu, R. K. Behera, M. Chen, L. Zhou, F. Liu, B. Wang, W. Huang, S. Zhang and L. Qi, *Small*, 2022, **18**, e2107799.
38 J. Kibsgaard and T. F. Jaramillo, *Angew. Chem., Int. Ed.*, 2014, **53**, 14433–14437.
39 Z. Luo, R. Nie, V. T. Nguyen, A. Biswas, R. K. Behera, X. Wu, T. Kobayashi, A. Sadow, B. Wang, W. Huang and L. Qi, *Nat. Commun.*, 2020, **11**, 4091.
40 Y. Huang, Z. Zeng, T. Wang and Z. Che, *Chem. Eng. J.*, 2025, **504**, 158543.
41 Q. Wan, L. Yuan, W. Jiang, Y. Liu, L. Zhang, X. Zhuang, J. Zhang and C. Ke, *ACS Sustainable Chem. Eng.*, 2023, **11**, 17046–17052.
42 Y. Wu, L. Charlesworth, I. Maglaya, M. N. Idros, M. Li, T. Burdyny, G. Wang and T. E. Rufford, *ACS Energy Lett.*, 2022, **7**, 2884–2892.
43 Y. Wu, S. Garg, M. Li, M. N. Idros, Z. Li, R. Lin, J. Chen, G. Wang and T. E. Rufford, *J. Power Sources*, 2022, **522**, 230998.